Vicarious calibration of MERIS over dark waters in the near infrared

Nadège Martiny*, Richard Santer, Irina Smolskaia

Laboratoire Interdisciplinaire des Sciences de l'Environnement (LISE), Université du Littoral Côte d'Opale, 32 Avenue Foch, 62930 Wimereux, France

Abstract

We propose to evaluate the calibration of MERIS (MEdium Resolution Imaging Spectrometer) over dark waters in the near infrared. We work with 5 months of data, from July to November 2003, over five world sites: Venice and Lampedusa in Italy, El Arenosillo in Spain, MOBY/Lanai and CalCOFI/San Nicolas in the United States. The sites are all equipped with a CIMEL station that forms part of the AERONET network. The basic idea is to associate CIMEL sky radiance measurements with MERIS level-1b data in a twin geometry which corresponds to the same scattering angle. This vicarious calibration relies on an accurate description of the atmospheric scattering based on the CIMEL measurements.

After a selection of MERIS and CIMEL data we finally obtained 8 days for the calibration task—about 10% of the initial dataset. We achieved a match-up analysis at 6 MERIS wavelengths, from 884 nm to 664 nm, in the near infrared (NIR). Results show an agreement between the onboard calibration and our method within 1.5% in the NIR which falls in the expected accuracy of the two methods.
© 2004 Elsevier Inc. All rights reserved.

1. Introduction

The physical interpretation of satellite data needs an accurate sensor calibration. An accuracy of a few percents is required for the radiometric calibration of ocean color missions. The calibration protocol usually includes a pre-launch radiometric activity as well as an onboard checking (Gordon, 1987). For this purpose, some of the ocean color sensors like MERIS (MEdium Resolution Imaging Spectrometer) or SeaWiFS (Sea-viewing Wide-Field-of-view Sensor) are equipped with diffuser panels (Barnes & Eplee, 1996) supposed to measure solar irradiance on a daily basis. Nevertheless, it is difficult to separate the degradation of the sensor calibration from a change in a panel reflectance. The lunar calibration (Kieffer & Widley, 1996) has been used additionally for SeaWiFS and MODIS (MODerate resolution Imaging Spectroradiometer) in order to indicate variations in the panel characteristics. This technique consists in assuming that the moon is a diffuse reflector whose surface remains unchanged. The sensor points at the moon each month in order to evaluate the temporal degradation of its sensitivity for each channel (Barnes et al., 1999).

For MERIS, launched on March 1, 2002, the primary calibration relies on the onboard panel. It is foreseen to use a twin panel, which is deployed occasionally to avoid degradation in the space environment, to cross-check with the panel used routinely. On the other hand, specific efforts have been devoted to vicarious calibration by different groups in response to the ENVISAT (ENVIronment SATellite) announcement of opportunity. Results of vicarious calibrations confirm that the onboard calibration lies within the uncertainties attached to the different methods. Combining the so-called Rayleigh calibration (Vermote et al., 1992) at short wavelengths to an inter-band calibration on the sun glint also confirmed the onboard calibration in the near infrared (Hagolle & Cabot, 2004). Other authors simulated the MERIS radiances over ocean using CIMEL ground-based extinction data as input to a radiative transfer code (RTC) and

* Corresponding author. Tel.: +0033 380393822; fax: +0033 380395741.

E-mail addresses: Nadege.Martiny@u-bourgogne.fr (N. Martiny), santer@mren2.univ-littoral.fr (R. Santer), smolskaia@muk.uni-hannover.de (I. Smolskaia).

illustrate that the sensor is calibrated with an accuracy of 2% in the near infrared (Antoine & Chami, 2004). Nevertheless, there is a debate on the calibration in the near infrared (NIR) because the inter-calibration of MERIS with other sensors (i.e., POLDER (POLarization and Directionality of the Earth's Reflectances) and SeaWiFS) over desert indicates a discrepancy of −7% to −10% with the onboard calibration (Hagolle & Cabot, 2004). On the other hand, recent studies also highlight discrepancies between MERIS and other sensors in the NIR. For instance, Nieke et al. (2004) inter-compared the outputs of three sensors: SeaWiFS, MERIS, and AVHRR (Advanced Very High Resolution Radiometer) over high-reflectance snow targets. CIMEL measurements, local weather information, and the spectral signature of "new snow" with no wavelength dependency in the NIR are used as input to a RTC to predict the top-of-atmosphere (TOA) radiance. The conclusion of their study is that the three sensors give consistent results within method uncertainty for 7 channels from 412 to 865 nm, but that the SeaWiFS radiance is lower than the MERIS radiance at 865 nm by 2.9%. Govaerts and Clerici (2004) compared the SEVIRI (Spinning Enhanced Visible and Infrared Imager) on board of MSG (Meteosat Second Generation) with four other space sensors: SeaWiFS, MERIS, ATSR-2 (Along-Track Scanning Radiometer-2), and VEGETATION over desert targets. The satellite measurements are compared with simulations using a surface reflectance data set (from POLDER and ATSR-2 measurements) and atmospheric properties derived from CIMEL data. Only data obtained in clear atmospheres, i.e., in the absence of dust storm events, are analysed. The results show that, whatever the instrument, the mean bias does no exceed 6% for all wavelengths. Compared with the SEVIRI/ MSG radiance, the MERIS radiance is on average higher by 5.5% and the SeaWiFS radiance lower by 1.8% in the near infrared. Consequently, it comes out that the SeaWiFS radiance is lower than the MERIS radiance by 7.3% on average. Moreover, Martiny et al. (submitted for publication) show that SeaWiFS has an onboard calibration lower by 7.0% on average in the NIR using the vicarious calibration method presented in the present paper. All these results tend to illustrate that SeaWiFS has an onboard calibration lower by several percents in the NIR, as well as POLDER, and that MERIS has an onboard calibration within the accuracy of the different calibration methods. We present here an independent method to calibrate MERIS in the NIR over water. Such a method has been proposed in the past (Parada et al., 1997) to calibrate AVIRIS (Airborne Visible InfRared Imaging Spectrometer) over Lake Tahoe in a traditional way that associated surface reflectance and solar extinction measurements to derive suitable inputs for simulations of the satellite signal. We suggest here a new methodology to calibrate MERIS in the NIR, based on the knowledge of the aerosol scattering (and not only the optical thickness) from ground-based measurements.

We start by general considerations on the radiometric calibration, pointing out that in this paper we use a calibration in normalized radiances because of the so-called smile effect of the instrument. We describe the general principle of this calibration, based on the direct association of the satellite signal with a ground-based measurement in the same scattering geometry. We explain how to improve the correspondence between upward and downward radiances using a RTC and an experimental determination of the phase function. Thereafter, for the calibration of the instrument, we are able to predict the MERIS incoming radiance by assuming that the atmospheric path radiance dominates the signal over the dark ocean in the NIR.

We present the obtained MERIS and CIMEL instruments databases and describe the selection process we applied. Regarding sky radiance measurements we illustrate the protocol used to account for temporal variability of the aerosols and for their spectral characteristics. Finally, we report our findings regarding the MERIS calibration.

2. Fundamental basis of radiometric calibration

MERIS (Rast et al., 1999) on ENVISAT is a programmable medium-spectral resolution imaging spectrometer operating in the solar reflective spectral range (400–900 nm). Fifteen spectral bands can be selected by ground command with a programmable width and spectral location (Merheim-Kealy et al., 1999). The scene is imaged simultaneously across the entire spectral range through a dispersing system onto a charge-coupled device (CCD) array. The programmed spectral width is obtained by summing the necessary number of CCD lines in the shift register. The CCD covers the spectral range with a nominal 1.25-nm spectral sampling interval. MERIS spectral bands are defined as the sum of one or more CCD detector pixel elements with a Full-Width Half-Maximum (FWHM) equal to 1.25 nm and a Gaussian response function for each element. The signal incoming to MERIS is a radiance L (W/ m^2/sr) integrated over the spectral response $S(\lambda)$ for a given detector (i, j) of the CCD matrix. Let us consider a specific MERIS band k which consists of the addition of different j columns depending on the band width. The corresponding radiance at band k is $L_k (j)$ and in order to normalize it by the filter response, we define an equivalent radiance L_k^e (W/ m^2/sr/μm) as follows:

$$L_k^e(j) = \frac{L_k(j)}{\int_0^\infty S_k(\lambda, j)\mathrm{d}\lambda}. \tag{1}$$

A spectral characterization has been performed before the MERIS launch during which spectral shifts have been observed, mainly due to the CCD integration with optics during the spatial registration. The so-called smile effect has a maximum spectral dispersion of 1.5 nm and can be observed at any wavelength. An onboard spectral calibration is based on the use of the pink panel that is an Erbium doped

panel with well-defined absorption peaks. In these absorption bands, each MERIS detector is spectrally characterized. This method is limited in the NIR because of the lack of absorption lines in the pink panel. The use of the Fraunhoffer lines gives complementary information in the violet and near infrared. Specific spectral band settings are used in the Fraunhoffer absorption lines during a limited number of orbits when observing the Earth. Spectral characterization is achieved within 0.1 nm of accuracy in accordance with most of the mission objectives (Delwart et al., 2003a).

A specific spectral arrangement is also used in the oxygen bands. Two different approaches are conducted: one based on the pressure retrieval and one based on the shape of the oxygen absorption. Both of them are first developed for clear skies land observations, but their performances are very similar for any type of targets. They also agree quite well within an accuracy of 0.02 nm. Full details are given in Delwart et al. (2003a).

During the onboard calibration the following calibration equation is applied:

$$L_k^e(j) = A_k(j)DC_k(j) \tag{2}$$

where, $A_k(j)$ is the calibration coefficient and DC the digital count recorded at band k on the j pixel. $L_k^e(j)$ corresponds to the sun signal reflected on the white panel of MERIS (spectralon). Introducing the mean solar irradiance $E_s^k(j)$ integrated on the spectral response of MERIS as:

$$E_s^k(j) = \frac{\int_0^\infty S_k(\lambda,j)E_s(\lambda)\mathrm{d}\lambda}{\int_0^\infty S_k(\lambda,j)\mathrm{d}\lambda}, \tag{3}$$

we get:

$$L_k^e(j) = \mu_s^k(j)\frac{E_s^k(j)}{\pi(d/d_m)^2}\rho_p^k(j) \tag{4}$$

where, $\mu_s^k(j)$ is the cosine of the solar zenith angle, ρ_p^k is the bi-directional reflectance of the white panel, d and d_m are the exact and mean Earth–Sun distances, respectively.

In order to apply Eq. (4), the bi-directional reflectance of the spectralon ρ_p^k is characterized at all MERIS bands k for each pixel j of each camera. $E_s^k(j)$ is computed using Eq. (3), with the extraterrestrial solar irradiance $E_s(\lambda)$ given in Thuillier et al. (1998).

The principle of the onboard calibration is fully described through Eqs. (2)–(4). Of course the calibration coefficient $A_k(j)$ depends on the MERIS band but also varies within the field-of-view (FOV).

In order to not require the knowledge of the solar irradiance $E_s^k(j)$ and consequently its variation within the FOV, because of the smile effect, we use the radiance L_k^* normalized by the solar irradiance defined as:

$$L_k^*(j) = L_k^e(j)\frac{\pi(d/d_m)^2}{E_s^k(j)}. \tag{5}$$

The values per pixel j of the solar irradiance $E_s^k(j)$ are reported in the MERIS auxiliary data file. The correction factor for the distance between the Earth and the Sun applied in Eqs. (4) and (5) is computed at the date of the measurement.

A calibration in normalized radiance over the spectralon will result in an equalization of the detectors on a CCD line. The detector equalization is achieved within a mean relative accuracy of 0.2% and peak to peak variation of 1% (Delwart et al., 2003b). Vicarious calibration can be conducted by reference to the onboard calibration in normalized radiance through:

$$L_k^\phi(j) = B_k L_{k,l1b}^\phi(j) \tag{6}$$

where, B_k is the calibration coefficient, $L_k^\phi(j)$ is derived from the vicarious calibration and $L_{k,l1b}^\phi(j)$ is the level-1b normalized radiance. The B_k coefficient does not depend on the j pixel because of the normalization of the radiance over the spectralon panel. A good MERIS calibration in the NIR would lead to a B_k coefficient of the magnitude of 1.

3. Principle of vicarious calibration in the NIR over dark waters

In this section we present the formulation of the TOA signal and we propose a vicarious calibration method that is based upon the correspondence between CIMEL ground-based measurements (both in extinction and diffusion) and MERIS data. This method, based on the correction of the multiple scattering effects in the atmosphere in order to be able working with the primary scattering approximation, is described theoretically in Santer and Martiny (2003) and has been applied once to the absolute calibration of SeaWiFS at 865 nm (Martiny et al., submitted for publication).

3.1. Correction of the multiple scattering effects at 865 nm

Over ocean, the TOA radiance received by a satellite can be expressed as follows (Gordon, 1997):

$$L_{TOA} = \big(L_{atm} + T*L_g + t*(L_w + L_{wc})\big)*T_g \tag{7}$$

where, L_{atm} is the radiance generated by the scattering in the atmosphere and by the specular reflection of the light scattered in the atmosphere, L_g is the signal generated by the specular reflection of the direct sun glint, L_{wc} is the contribution arising from the light reflection on the white-caps at the sea surface, and L_w is the water leaving radiance. The terms T and t are the direct and diffuse atmospheric transmittances, respectively, and T_g is the gaseous transmittance assumed to be decoupled from the scattering. Different assumptions can simplify Eq. (7):

(i) L_w is generally equal to zero in the near infrared over dark waters,

(ii) L_{wc} is negligible if the wind speed is smaller than 10 m/s, and

(iii) L_g is equal to 0 if we avoid the sun glint.

Table 1 is a list of the NIR MERIS bands and gives for a *Mid-Latitude Summer* profile (McClatchey et al., 1971) correspondent ozone and Rayleigh optical thicknesses, together with transmissions for water vapor, oxygen, and ozone (Tanré et al., 1990). We excluded the 761-nm oxygen band as well as the 900-nm water vapor band because of the strong influence of the gaseous absorptions. Gaseous transmission computations indicate that the 708-nm band is slightly contaminated by water vapor. In principle, if it is possible to correct for the water vapor absorption, in practise this correction is quite difficult because over dark targets, (i) we need to couple scattering and absorption, (ii) we need to account for the smile effect, and (iii) we need to input the water vapor content which is not accurately known. For the above reasons we do not perform the vicarious calibration at 708 nm. It is not critical because our main goal is to check the onboard calibration in the NIR and discrepancies between vicarious and onboard calibrations should vary continuously with wavelength. For the NIR bands under consideration we apply an ozone absorption correction using the optical depth reported in Table 1 weighed by the ozone content taken from MERIS auxiliary files.

After the ozone correction we just need to determine the atmospheric path radiance. The fundamental basis is to associate the atmospheric path radiances as measured from space and from the ground corresponding to the schematic representation in Fig. 1. In a primary scattering approximation and at a same scattering angle, we can write:

$$L^u = L^d \frac{\mu_v^d}{\mu_v^u} \qquad (8)$$

where, L^u is the upward radiance observed from space and L^d the downward radiance observed from the ground. The proportionality factor is the ratio between the two air masses that is expressed by the ratio between the downward cosine μ_v^d and the upward cosine μ_v^u of the view angles. At a same scattering angle Θ, the downward
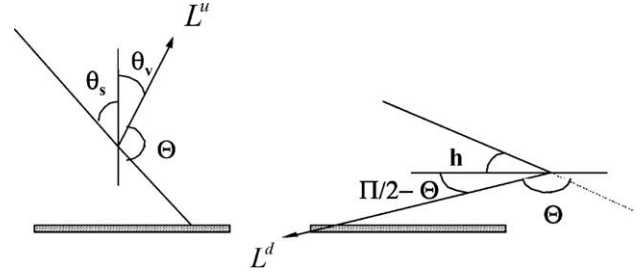

Fig. 1. Geometric correspondence between the atmospheric path radiance L^u as measured from space and the downward atmospheric radiances L^d as measured from the ground. The twin observations correspond to the same scattering angle Θ. From space, the solar and view zenith angles are noted θ_s and θ_v, respectively. From the ground, h corresponds to the solar elevation and $(\pi/2-\theta)$ to the complementary angle of the downward view zenith angle.

or upward radiances used in Eq. (8) are simply related to the atmospheric phase function P as:

$$L = \frac{\tau_{tot} * P(\Theta)}{4\mu_v}, \qquad (9)$$

where τ_{tot} is the total optical thickness and μ_v the cosine of the view zenith angle (downward or upward). Using Eqs. (8) and (9) we neglect the multiple scattering effects so we do not take into account the coupling between the Fresnel reflection at the sea surface and the atmospheric scattering.

Of course, the downward radiances measured by the CIMEL instrument include the multiple scattering effects. In order to be able working with the primary scattering approximation and use Eqs. (8) and (9) to predict the TOA signal from the CIMEL measurements, we first have to correct the sky radiances for the multiple scattering effects. This correction is done using the *f*-factor defined in Santer & Martiny (2003) as:

$$f = \left(\frac{L^{(1)}}{L}\right)_{theo} \approx \left(\frac{L^{(1)}}{L}\right)_{mes} \qquad (10)$$

where, $L^{(1)}$ stands for the primary scattering radiance in the atmosphere and L for the multiple scattering radiance. The *f*-factor, that is a ratio between downward radiances, is not very sensitive to the aerosol model so our scheme is based on its iterative estimate. Nevertheless, we need to make the

Table 1
Optical thicknesses and transmissions of the main absorbers in the NIR MERIS bands

Band	λ (nm)	$\Delta\lambda$ (nm)	δ_{O_3}	δ_r	Absorbers	T_{H_2O}	T_{O_2}	T_{O_3}
7	665	10	1.64E-02	4.50E-02	O_3	1.0000	1.0000	0.9838
8	681.25	7.5	1.15E-02	4.10E-02	$H_2O + O_3$	0.9995	1.0000	0.9886
9	708.75	10	6.30E-03	3.50E-02	$H_2O + O_3$	0.9675	1.0000	0.9937
10	753.75	7.5	3.06E-03	2.70E-02	$H_2O* + O_3$	0.9997	1.0000	0.9969
12	778.75	15	2.46E-03	2.40E-02	$H_2O* + O_2$	0.9996	0.9985	0.9975
13	865	20	7.02E-04	1.50E-02	H_2O*	0.9990	1.0000	0.9993
14	885	10	3.88E-04	1.40E-02	H_2O	0.9920	1.0000	0.9996

δ_{O_3} and δ_r stand for the ozone and Rayleigh optical thicknesses, respectively. T_{H_2O}, T_{O_2}, and T_{O_3} correspond to the water vapour, oxygen, and ozone transmissions, respectively. The values are computed for a *Mid-Latitude Summer* profile, a solar zenith angle of 30° and a nadir view. H_2O* denotes the water vapour continuum.

assumption of an aerosol model to estimate f at order 0. The aerosol size distribution chosen to start the iterative procedure is a simple Junge size distribution defined from the CIMEL extinction measurements: aerosol optical thickness τ_a and spectral dependency α between two wavelengths λ_1 and λ_2 expressed as:

$$\alpha(\lambda_1, \lambda_2) = \ln[\tau_a(\lambda_1)/\tau_a(\lambda_2)]/\ln(\lambda_1/\lambda_2). \tag{11}$$

$L^{(1)}$ and L are obtained using the successive-order-of-scattering (SOS) code developed by Deuzé et al. (1989), previously validated in an extensive inter-comparison (Dilligeard et al., 2002) with the matrix operator method (MOMO) code (Fell & Fischer, 2001), because it has been used to generate the look up tables needed in the MERIS level-2 algorithms and thus gives a full consistency within the MERIS level-2 production.

This version of SOS corresponds to a plane parallel atmosphere bounded by the ocean. We assume that the ocean body is dark and we consider that the Fresnel reflection is associated to the wave slope distribution proposed in Cox and Munk (1954). Although there are some uncertainties related to the latter term, we can assume that the Cox and Munk model versus the wind speed provides the required accuracy to account for the coupling between Fresnel reflection and atmospheric scattering. In the NIR the polarization impacts a little on the computation of the total radiance because it occurs only when multiple scattering is present. The RTC runs in a vector mode, what means that we can take the polarization into account. Computations indicate that it is relevant to include both the Rayleigh scattering and the Fresnel reflection polarization but not necessarily that of aerosols.

Only a few iterations (3 to 5) are needed to converge within 0.5% on the f-factor.

3.2. Computation of aerosol phase function from sky radiance measurements at 865 nm

At each step the f-factor is calculated, the radiances measured in the principal plane (PPL) by the CIMEL instrument are corrected for the multiple scattering effects and the $\omega_o P(\Theta)$ product (single scattering albedo time phase function) is obtained using the exact primary scattering formulation for a homogeneous atmosphere:

$$\omega_o P(\Theta) = 4L^{(1)} \exp\left(\frac{\tau_{tot}}{\mu_v}\right) \left[1 - \exp\left(-\tau_{tot}\left(\frac{1}{\mu_s} - \frac{1}{\mu_v}\right)\right)\right]^{-1}$$
$$\times \left[\frac{\mu_s}{\mu_v - \mu_s}\right]^{-1}, \tag{12}$$

where, μ_s is the cosine of the solar zenith angle θ_s. The $\omega_o P(\Theta)$ product is then expanded into Legendre polynomials using a Gaussian quadrature. The integration is done for a scattering angle Θ between $0°$ and $180°$. The PPL measurements cover the scattering angle range $(0°, 90°+\theta_s)$. The greater the solar angle θ_s is, the less we have to extrapolate the phase function at large scattering angles in order to compute Legendre polynomials. This extrapolation is done using the Junge size distribution associated to the aerosol optical thickness (AOT).

The angular integration of the $\omega_o P(\Theta)$ product gives the ω_o value. The Rayleigh scattering is conservative so we get:

$$\omega_o = \frac{\tau_a \omega_o^a + \tau_r}{\tau_a + \tau_r}, \tag{13}$$

from where knowing the aerosol optical thickness τ_a and the Rayleigh optical thickness τ_r we get the aerosol single scattering albedo ω_o^a. The product $\omega_o P(\Theta)$ corresponds to the mixture of aerosols and molecules and we write $\omega_o P(\Theta)$ as:

$$\omega_o P(\Theta) = \frac{\omega_o^a \tau_a P_a(\Theta) + \tau_r P_r(\Theta)}{\tau_a + \tau_r}. \tag{14}$$

Using Eq. (14) and knowing the Rayleigh phase function $P_r(\Theta)$ we can deduce the aerosol phase function $P_a(\Theta)$. The aerosol parameters derived from CIMEL extinction measurements, τ_a, and CIMEL sky radiances, ω_o^a and P_a, are used as the inputs into a RTC to predict the MERIS normalized TOA radiance.

The method of Santer and Martiny (2003) is inspired from the one of Gordon and Zhang (1996) who proposed an absolute calibration for SeaWiFS at 765 and 865 nm using ground-based solar extinction and sky radiance measurements at the time of satellite overpass. Instead of iterating directly over phase function and single scattering albedo, Santer and Martiny propose to iterate directly on the f-factor defined in Eq. (10). In both methods the authors show that the TOA radiance measured by satellites, L_{TOA}, could be accurate at 1% or 2% in the NIR if the ground-based radiometer is perfectly calibrated.

In Martiny et al. (submitted for publication) a detailed error budget is conducted for the vicarious calibration methodology described above. It is shown that the inaccuracy of the method is mainly due to uncertainties in the retrieval of the phase function from the CIMEL ground-based measurements, $\pm 0.6\%$ to $\pm 2.2\%$ depending on angular geometry, atmospheric transmittance, $\pm 0.6\%$, aerosol polarization, $\pm 1\%$, and radiation transfer modelling, $\pm 1.2\%$. This gives for L_{TOA} a total error budget of $\pm 2.0\%$ to $\pm 3.6\%$, in which individual uncertainties have been added quadratically. As previously mentioned most of the uncertainty in the retrieval of the phase function is due to the radiometric calibration of the CIMEL instruments, assumed to be accurate to $\pm 2\%$ in the near infrared (Meister et al., 2003).

4. Database

From space we observe the backscattering part of the phase function. From the ground we can not have access to

the same geometry as at the satellite time of overpass. The association is not simultaneous, what supposes to account for possible temporal variability.

(i) From the ground, Eq. (8) becomes invalid for large sun and view zenith angles. Practically a 75° angle is a maximum that corresponds to a scattering angle Θ of 150° for an observation in the principal plane.
(ii) Then only spatial observations corresponding to $\Theta \leq 150°$ are accounted for.
(iii) The geometry for the ground-based is possible in the early morning, and thus, for relatively large aerosol optical thickness. We paid attention using only days for which the early morning optical thickness was not too high in order to correct more easily for the multiple scattering effects. Aerosol optical thicknesses are always lower than 0.3 at 550 nm what approximately corresponds to a visibility greater than 23 km.

For the database we selected five test sites (see Fig. 2) for which there were both CIMEL and MERIS measurements from July to November 2003. These sites are: Venice (45.30°N, 12.50°E), El Arenosillo (37.11°N, 6.71°W), Lampedusa (35.52°N, 12.62°E), MOBY (20.82°N, 156.98°W), and CalCOFI (33.25°N, 119.48°W).

The first criteria applied on CIMEL data is based on the relative stability of the aerosol optical thickness during the day. The maximum variability accepted is set to 0.07 at 865 nm and 0.09 at 443 nm. In these conditions the Angstroem coefficient α may not be stable during the day, what implies a non conservative aerosol model. Secondly, we keep CIMEL data in coincidence with MERIS measurements with an upward scattering angle lower than 150°. For this purpose, we need to check that measurements in the principal plane exist in the early morning. In addition, we have to check that there are regular measurements in the principal plane during the morning in order to increase the chance of having sky radiance measurements around the MERIS time of overpass. Above CIMEL selection criteria

are quite severe and as a result we retain about 20% of the initial dataset.

The initial MERIS dataset is constituted of 82 clear sky images over the five test sites from July to November 2003. We use the following selection criteria:

(i) We only select images where both MERIS and relatively stable AOT derived from ground-based CIMEL measurements exist.
(ii) We display the sun glint flag to inspect the sun glint effect then we select the images for which the CIMEL site is within the area either not contaminated by glint or with low glint because this term is difficult to model (see Eq. (7)).
(iii) To have a good spatial homogeneity we display an image at 865 nm and we inspect a transect in the area of the CIMEL station for level-1b data.
(iv) In order to identify possible clouds we firstly examine the level-1b MERIS image at 865 nm. Secondly, to check for cirrus clouds, we display the (760 nm/753 nm) ratio image representative of the oxygen absorption and we inspect a transect in the area of the CIMEL station.

We illustrate the processing for a MERIS scene on October 25, 2003 over the Venice site. In the MERIS images of Fig. 3 we mark the coastline in red with an accuracy of about 500 m and we plot a transect perpendicular to the coast indicated by a blue arrow. Fig. 3a shows a glint flagged RGB MERIS image acquired on this day. It is easy to see that there is no glint present, which is not always the case. Fig. 3b shows the graph presenting values of TOA radiance at 865 nm along the transect indicated in Fig. 3a. At 865 nm the values are high at the beginning of the transect because of the brightness of the land. Then, within the first few kilometres at sea, we can clearly observe the adjacency effects due to the land proximity. We pay attention here and try to avoid areas where there are structures on the water. Then moving along the transect we
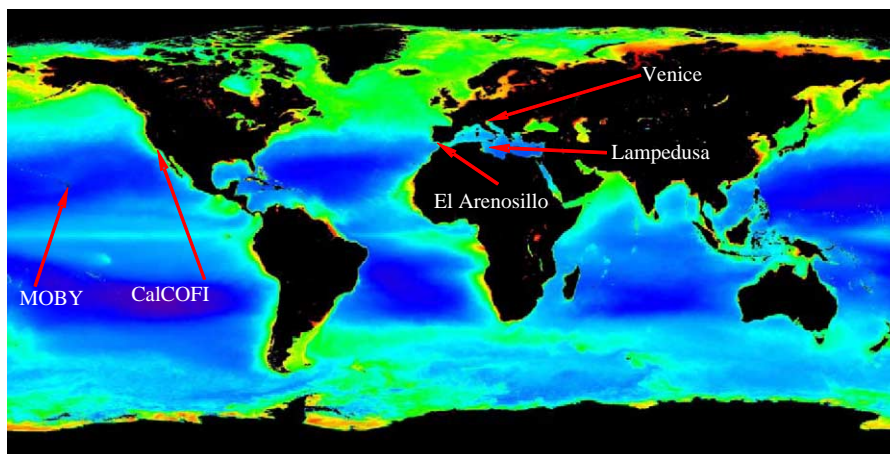

Fig. 2. Location of the five test sites selected. The world map used in the background is taken from http://seawifs.gsfc.nasa.gov.
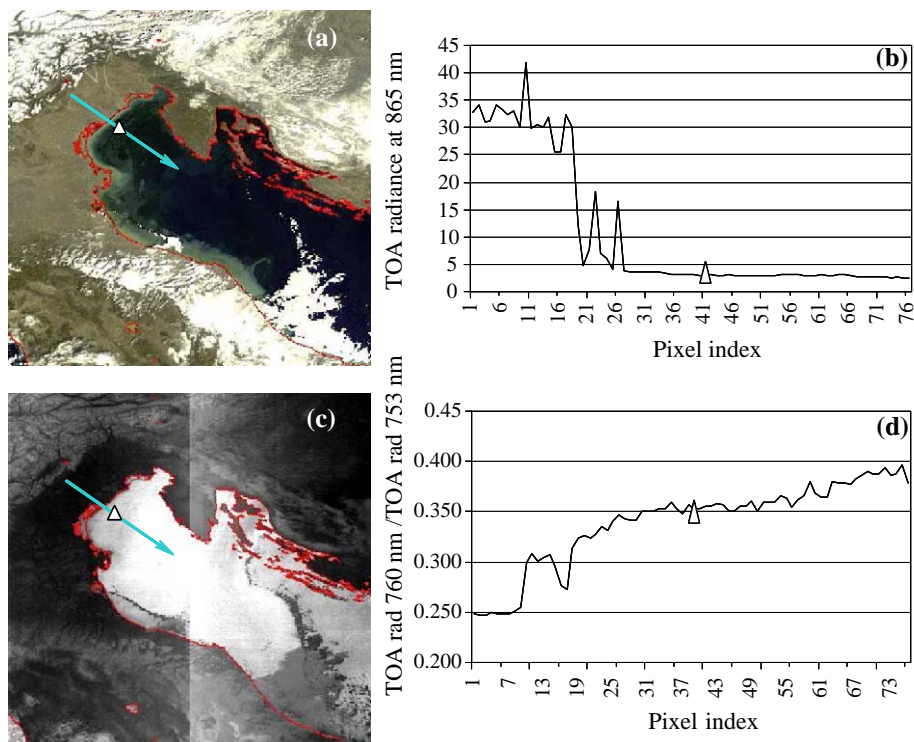
Fig. 3. Illustration of the selection protocol applied to MERIS data on October 25 over the Venice site. Panel (a) shows the MERIS RGB image we used to display the sun glint mask and to visualize clouds. The blue arrow indicates the direction of the transect used to identify the area nearby the CIMEL station from where level-1b TOA radiances are selected. Panel (b) shows the MERIS TOA radiance at 865 nm in (mW/m^2/sr/nm) along the transect. The image of the two bands ratio 760 nm/753 nm, shown in panel (c), is used to emphasize the presence of cirrus clouds. It is possible to see the camera interface due to the so-called smile effect. The blue arrow indicates the direction of the transect. Panel (d) demonstrates that no cirrus clouds were detected along the transect. (For interpretation of the references to colour in this figure legend, the reader is referred to the web version of this article.)

cross the Venice tower where the signal becomes stable and does not change until the end of the transect. For the study we always aim at finding areas with nearly constant TOA radiances and, in such a case, we open a small 3×3 pixels window for which we extract averaged TOA radiances. Fig. 3c shows the MERIS image representing the (760 nm/753 nm) TOA radiances ratio which is very sensitive to the presence of cirrus clouds. Fig. 3d shows the graph

presenting values of this oxygen bands ratio along the transect indicated in Fig. 3c. Few tenths of kilometres around the station location, indicated by a triangle in the plot, the ratio is equal to 0.37 on average with a variation of ±0.02. If we split the transect into two parts: one part before the station (land-station trajectory) and the other after the station (station-sea trajectory), we can state that the minimum value of the ratio is 0.35 in the land-station

Table 2
Aerosol characteristics of the 13 days initially selected

Site	Date [overpass time]	τ_a (870 nm) [overpass]	τ_a (870 nm) [daily average]	α (NIR) [overpass]	α (NIR) [daily average]
CalCOFI	Oct. 25, 18:12:13	0.06	0.06±0.02	−1.3	−1.2±0.1
	Oct. 28, 18:18:15	0.05	0.06±0.03	−1.3	−1.5±0.2
	Nov. 10, 18:10:55	0.05	0.06±0.01	−0.5	−0.5±0.1
Lampedusa	Aug. 20, 9:20:24	0.21	0.23±0.07	−1.1	−1.5±0.4
MOBY	Oct. 27, 20:30:23	0.30	0.30±0.02	−0.8	−0.8±0.1
Venice	Aug. 10, 9:34:42	0.15	0.19±0.04	−1.4	−1.4±0.2
	Aug. 13, 9:40:18	0.21	0.18±0.03	−1.8	−1.7±0.1
	Aug. 23, 9:45:59	0.21	0.19±0.02	−1.7	−1.8±0.1
	Oct. 25, 9:49:11	0.05	0.05±0.01	−1.6	−1.8±0.2
	Nov. 4, 9:35:49	0.05	0.05±0.01	−1.7	−1.5±0.2
	Nov. 7, 9:41:52	0.06	0.06±0.02	−1.6	−1.3±0.3
	Nov. 10, 9:47:54	0.04	0.06±0.02	−1.3	−1.1±0.2
	Nov. 13, 9:53:55	0.11	0.11±0.01	−1.6	−1.6±0.1

For each day we give the MERIS time of overpass and the corresponding CIMEL aerosol optical thickness and Angstroem coefficient in the NIR. The daily average values of AOT and α are also reported with their absolute variation.

portion and that the maximum value of the ratio is 0.39 in the station-sea portion. Consequently, no significant variation is observed comparing to the sensitivity of this ratio to the presence of clouds. This confirms that there are no cirrus clouds on October 25, 2003.

Finally, after the above mentioned selection process we obtain a total of 13 days over four sites that are listed in Table 2. This data represent 16% of the initial dataset. Most of the selected days are exceptionally clear even if 5 days have greater AOT, of the magnitude of 0.15 at 865 nm. A large majority of days present high spectral dependency and only three of them have an Angstroem coefficient of the magnitude of −0.5—one over CalCOFI, one over Lampedusa and one over MOBY. As a small aerosol spectral dependency is usually associated to a strong forward peak of the aerosol phase function, we may need for these days to truncate the phase function derived from the early morning PPL measurements. This is fully explained in the section below.

5. Retrieval of phase functions from the sky radiances at 865 nm, temporal variability

The derivation of the phase function is done at 865 nm because CIMEL measurements are more sensitive to aerosols at this wavelength due to the low Rayleigh contribution. We decide to work with the first sequence of sky radiances, collected in the early morning in the principal plane, to determine the phase function covering a large range of scattering angles. As MERIS overpasses the sites in middle of morning there is a time gap between the phase function derivation and satellite measurements. Thus, we recommend checking the "early morning" phase function for different scenarios we scale between 1 and 3: when there are no PPL measurements around the MERIS overpass, the quality index is set to 3; it is set to 2 when an other PPL sequence exists but with a time gap greater than 1 h between MERIS measurements and the closest PPL measurements; it is set to 1 when there are two PPL measurements surrounding the MERIS overpass.

We check here the temporal stability of the "early morning" phase function P by simulating with it the PPL radiances for the PPL sequence closest to the MERIS overpass. Although the AOT should be stable during the day because of the CIMEL data filter described in the previous section, we have to account for its small variation from the time of "early morning" phase function derivation to the time of MERIS overpass. Like this, the eventual discrepancies between the simulations of PPL closest to the MERIS overpass and the associated measurements at 865 nm may be due to the variation of the aerosol phase function. We present now two examples of the possible temporal variability of the "early morning" phase function.

There are some cases for which there is no discrepancy between the PPL sequences closest to the MERIS overpass

and corresponding simulations, what means that the "early morning" phase function is really stable. For instance, October 25, 2003 over CalCOFI is particularly stable. The "early morning" phase function has been derived at 16:51 local time and used to retrieve PPL measurements at 17:51 and 18:51 since MERIS overpasses the site at 18:12. In this case the quality index is set to 1. Moreover the PPL measurements at 17:51 and 18:51 cover the MERIS scattering angle that is about 129°. At this angle the retrieval of sky radiance measurements is performed within 0.5% (see Fig. 4) indicating that there is no ambiguity about the suitability of the phase function derived from "early morning" sky radiance measurements. The large discrepancies observed between measurements and simulations for small scattering angles (lower than 5°) are the results of the truncation of the "early morning" phase function. Indeed, once we derive the aerosol phase function P_a from PPL measurements, we have to decompose it at cosines of Gauss angles μ into Legendre polynomials β_l weighted by p_l as follows:

$$P_a(\mu) = \sum_{l=0}^{\infty} \beta_l p_l(\mu), \tag{15}$$

in order to obtain the proper inputs to the SOS RTC. At this stage a checking of the decomposition is done by reconstituting the aerosol phase function from the derived Legendre polynomials by step of 1°. Oscillations of the phase function can be observed what means that the 80 Legendre polynomials usually used for the decomposition of P_a are not sufficient to properly characterize the phase function, especially in the forward peak. There are two ways of going round this problem: either to increase the number
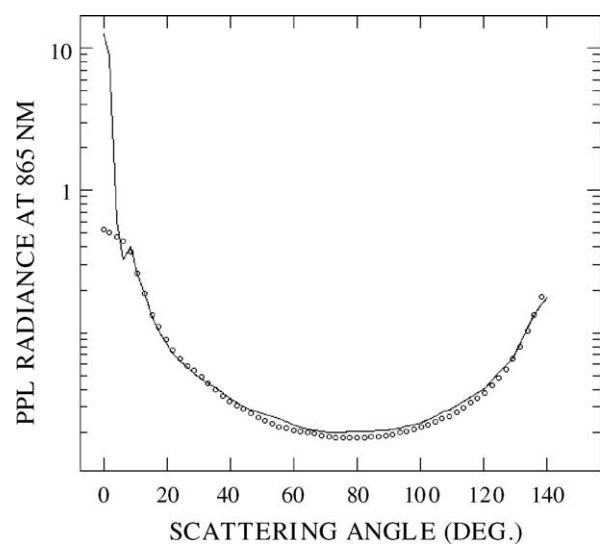

Fig. 4. Example of PPL radiances simulation (○) using the "early morning" phase function at 865 nm to retrieve PPL measurements close to the MERIS overpass. On October 25, 2003 over CalCOFI the airmass was very stable and we perfectly retrieve (see text) the CIMEL sky-radiance measurements (—) at 17:51 local time with the phase function derived 1 h before.
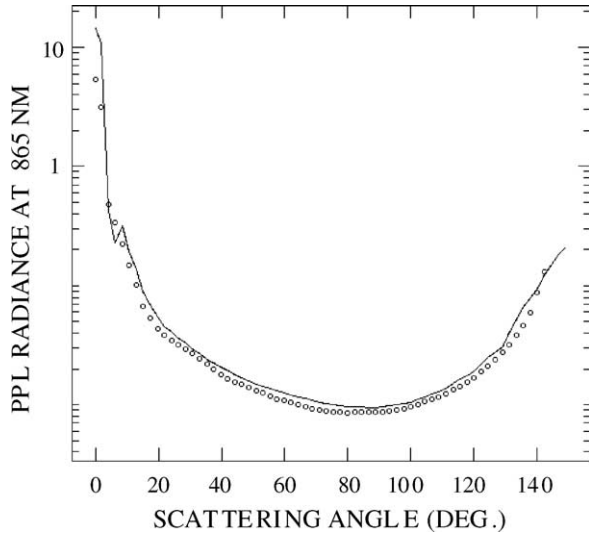
Fig. 5. Same as Fig. 6 but on October 28, 2003 over CalCOFI. We do not exactly retrieve (see text) the CIMEL sky-radiance measurements at 17:51 local time with the phase function derived two hours before. In such a case we have to apply Eq. (16) defined in the text.

PPL measurements and downward radiance simulations at 17:51 is about 22.1%. At 18:51 the difference is similar since it reaches 22.5%. Thus, we interpolate these results by taking into account the exact time of MERIS overpass (18:18) and we obtain a ΔL^d difference of 22.3%.

As we have already considered the variation of AOT in the computations this discrepancy is the actual variation of the phase function from its time derivation in the early morning to the time of MERIS overpass. A change in the aerosol phase function is a consequence of a change in the aerosol model during the morning. Considering the AOT filter applied on the CIMEL data, we have to show that 20% is a possible magnitude for the downward sky radiance difference ΔL^d. Among the 13 days selected, the Angstroem coefficient can have a maximum variation of ± 0.4 during the day (see Table 2). For instance, on October 28, 2003 the Angstroem coefficient has a variation of +0.4 from the early morning (16:06 local time) to the MERIS overpass (18:18 local time). Let us simulate the phase functions at 16:06 and around the MERIS overpass using the Mie theory and assuming a simple Junge size distribution associated to CIMEL Angstroem coefficients as the aerosol models. At a $122°$ scattering angle (geometry of the October, 28 MERIS image) the simulated phase functions at 16:06 and 17:51 are equal to 0.2318 and 0.1839, respectively. This means that the relative difference between both is about 21% that is a coherent value with the magnitude of ΔL^d found out on October, 28 over the CalCOFI site. Of course, the retrieval of aerosol phase functions using Junge size distributions is a crude approximation. Consequently, this exercise allows illustrating the possible variation of the downward sky radiances during the morning implied by the modification of the aerosol model. Nevertheless, it cannot be used for the accurate exercise of the MERIS vicarious calibration in the NIR. On October, 28 no truncation of the phase function

of Legendre polynomials or to truncate the forward peak of the phase function. We choose the latter solution in order to optimize the computation time. The truncation of the phase function is always coupled with the truncation of the aerosol optical thickness and the aerosol single scattering albedo.

We present now the second example of the "early morning" phase function temporal variability (see Fig. 5). On October 28, 2003 the "early morning" phase function has been derived at 16:06 local time and we have two PPL sequences surrounding the MERIS overpass: one at 17:51 and another at 18:51. The quality index is again set to 1. In both cases, at 17:51 and 18:51, the MERIS scattering angle (122°) is covered by PPL measurements. At this scattering angle, the relative difference between

Table 3
Sky radiance characteristics of the 13 days initially selected

Site/Date	t_{CIMEL}	t_{PPL1}	t_{PPL2}	t_{MERIS}	Index	Θ (°)	$(\Delta L^u/L^u)_{13}$ (%)	$(\Delta L^u/L^u)_7$ (%)
CA1025	16:51	17:51	18:51	18:12	1	129.	0	0
CA1028	16:06	17:51	18:51	18:18	1	122.	+17.3	+6.4
VE1104	8:03	9:02	10:02	9:35	1	120.	0	−7.2
VE1113	8:07	9:02	10:02	9:53	1	104.	−10.1	−8.2
CA1110	17:51	–	18:51	18:10	2	128.	0	−6.9
VE0810	6:10	8:17	–	9:34	2	146.	0	−5.3
VE0813	6:17	–	10:22	9:40	2	139.	0	−14.0
VE1025	9:02	–	10:02	9:49	2	112.	0	−7.4
VE1107	9:02	–	10:02	9:41	2	115.	+5.4	+3.0
VE1110	9:02	–	10:02	9:47	2	110.	−9.0	−8.1
LP0820	6:22	–	–	9:20	3	150.	–	–
MB1027	18:07	–	–	20:30	3	136.	–	–
VE0823	6:28	–	–	9:23	3	150.	–	–

Each day is denoted by the two first letters of the site's name, the month and day of the MERIS overpass. The reported t_{CIMEL}, t_{PPL1}, t_{PPL2} parameters are times corresponding to the "early morning", the "before MERIS overpass", the "after MERIS overpass" CIMEL PPL measurements, respectively. The MERIS time overpass is indicated as t_{MERIS}. The consequently quality index is given. The MERIS scattering angle Θ is also reported as an indicator. For this angle we report the relative difference between the MERIS measurements and TOA radiances, simulated with the "early morning" phase function derived from PPL measurements, at MERIS bands 13 and 7.

was required, that is why the retrieval of the forward peak is better performed than on October, 25 over the CalCOFI site.

When a ΔL^d difference exists we have to take it into consideration for the retrieval of MERIS TOA radiances. The ΔL^d difference is used to compute a corrective factor applied to upward radiances simulated with the "early morning" P phase function. According to Eq. (8) we simply correct L^u using the following approximation:

$$\Delta L^u = \Delta L^d \frac{\mu_v^d}{\mu_v^u}. \tag{16}$$

In Table 3 we summarize different parameters related to CIMEL sky-radiance measurements realized for the 13 days

selected: the times of the "early morning", "before MERIS overpass" and "after MERIS overpass" PPL measurements (t_{CIMEL}, t_{PPL1}, and t_{PPL2}, respectively) and the time of MERIS overpass (t_{MERIS}). The resulting quality index is also indicated together with the $\Delta L^u/L^u$ ratio computed at 865 nm as follows:

$$\frac{\Delta L^u}{L^u} = \frac{L_{MERIS}^u - L_{CIMEL}^u}{L_{CIMEL}^u}. \tag{17}$$

To compute L_{CIMEL}^u at 865 nm we use the "early morning" phase function at 865 nm as an input into the RTC. L_{MERIS}^u is the normalized MERIS TOA radiance at 865 nm (band 13). The definition of the ratio $\Delta L^u/L^u$ is only
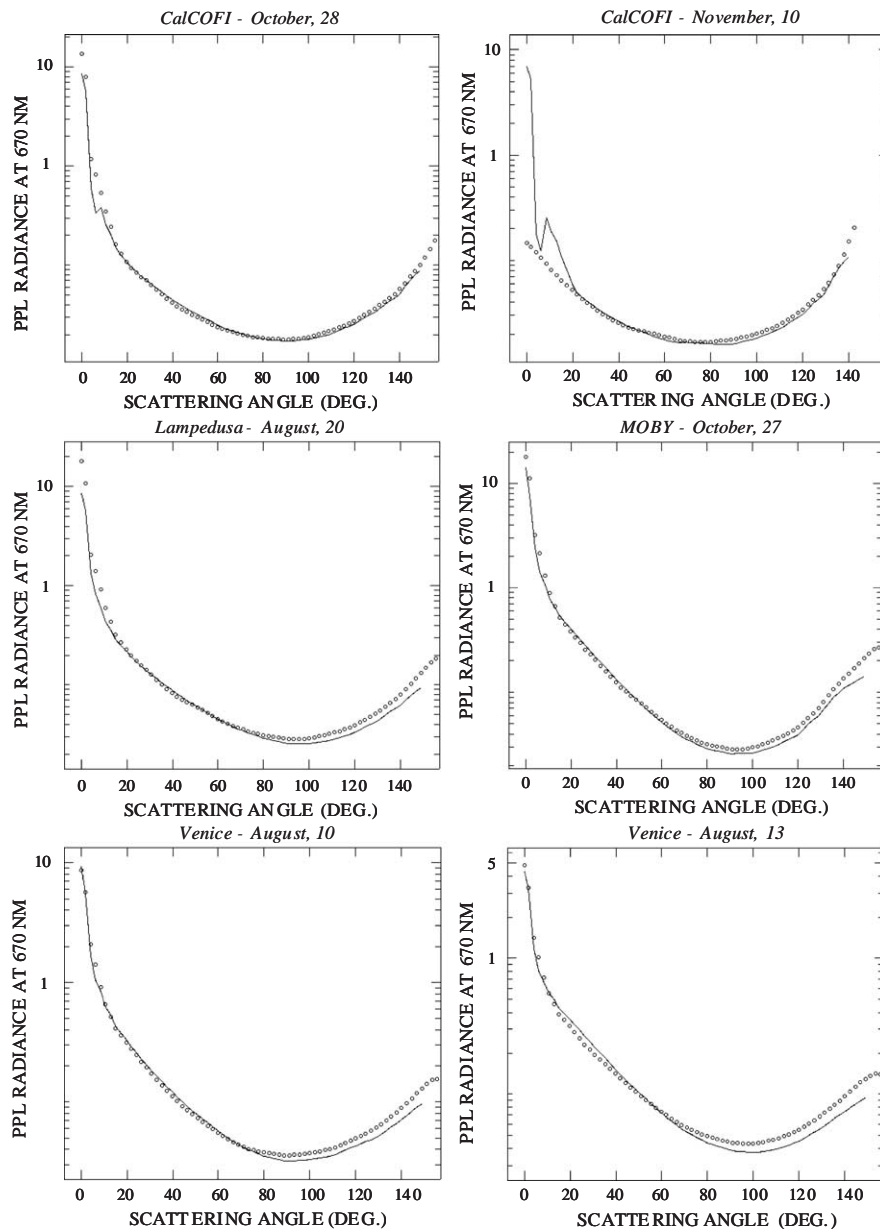

Fig. 6. Spectral variation of the aerosol phase function from the NIR to Red part of the spectrum. The "early morning" phase function derived from the CIMEL sky-radiance measurements at 865 nm is used to simulate the sky-radiances at 670 nm that we compare to ground-truth measurements at the same wavelength. We report six comparisons on which site and date are labelled.

possible when the index is set to 1 or 2. At 865 nm, it is equal to 0 for half of the days. Otherwise, it can be positive or negative and it can reach the absolute value of 17.3% (see Table 3). In these cases it means that there is a slight variation of the aerosol model from the early morning to the middle morning (overpass of MERIS).

6. Retrieval of phase functions at MERIS NIR bands, spectral dependency

By now, we only have computed the atmospheric phase function $P(\Theta)$ from CIMEL sky radiance measurements at 865 nm. We would like to have this phase function at all NIR MERIS bands which means that we have to derive aerosol parameters, ω_o^a and $P_a(\Theta)$, at all wavelengths in order to apply Eq. (8) to predict MERIS L^u. For this purpose, we could use the following protocol:

(i)   We have ω_o^a and $P_a(\Theta)$ at 865 nm from $P(\Theta)$ using Eqs. (13) and (14).
(ii) We also extract ω_o^a and $P_a(\Theta)$ at 670 nm.
(iii) Then, we interpolate ω_o^a and $P_a(\Theta)$ at each NIR MERIS band.

The problem is that the extraction of the phase function at 670 nm from CIMEL sky radiance measurements is more critical than at 865 nm. Indeed the signal measured by the radiometer at this wavelength is less sensitive to the aerosols than at 865 nm because of the more important Rayleigh contribution. Moreover, the ocean is not completely absorbent anymore and the contrast between the land and the sea is important what emphasizes the environment effects. All this together makes the derivation of the phase function at 670 nm a bit more delicate than at 865 nm.

An alternative method to predict L^u at all MERIS NIR bands is to always use ω_o^a and $P_a(\Theta)$ at 865 nm as the input of the SOS RTC, instead of using ω_o^a and $P_a(\Theta)$ at other NIR wavelengths, but on the other hand to evaluate the $\Delta P_a(\Theta)$ variation from 865 to the other NIR bands. According to Eq. (9) that relies on the primary scattering approximation, and introducing the AOT measured at the time of the MERIS overpass, we can assume:

$$\Delta L^d = \frac{\tau_a \Delta P_a(\Theta)}{4 \mu_v^d}. \tag{18}$$

We first evaluate ΔL^d at 670 nm comparing CIMEL sky radiance measurements to PPL radiances simulated using $\omega_o^a P_a(\Theta)$ at 865 nm. In Fig. 6 we present the retrievals for several days of the "early morning" PPL measurements at 670 nm using the phase function at 865 nm. The days presented are chosen among the 13 days summarized in Table 2. We can see that the relative difference between CIMEL measurements and simulations at the MERIS

scattering angles can vary between 7% and 18%. From ΔL^d at 670 nm and using Eqs. (16) and (17) we get $\Delta L^u / L^u$ at 670 nm (see Table 3). This ratio is rarely equal to 0 and it can either be positive or negative reaching sometimes the absolute value of 14.0%. Knowing $\Delta L^u / L^u$ at 865 nm and 670 nm we can interpolate $\Delta L^u / L^u$ at all MERIS NIR bands and we can express $L_{final}^u(\lambda_{NIR})$, the simulated upward radiance at a NIR wavelength λ_{NIR} after correction as follows:

$$L_{final}^u(\lambda_{NIR}) = L^u(\lambda_{NIR}) + L^u(\lambda_{NIR}) \frac{\Delta L_u(\lambda_{NIR})}{L_u(\lambda_{NIR})}, \tag{19}$$

where $L^u(\lambda_{NIR})$ is the upward radiance at λ_{NIR} simulated using the "early morning" phase function at 865 nm. As a result for simulation of MERIS TOA radiances, we do not have to derive the $\omega_o^a P_a(\Theta)$ product at all MERIS NIR bands but instead, we can simply use $\omega_o^a P_i(\Theta)$ at 865 nm, and if required, estimate $\Delta P_a(\Theta)$ from 865 nm to all MERIS NIR wavelengths through the estimate of ΔL^d as described in Eq. (18).

7. Simulation of MERIS TOA radiances

We have 13 days selected over four sites from July to November 2003 for the vicarious calibration of MERIS in the NIR. Two of them have been removed (October, 25 over CalCOFI and November, 7 over Venice) because the CIMEL sites were covered or surrounded by clouds on the MERIS images. This means that the instabilities were really furtive for these days and that they could not be detected by the AOT measurements.

The MERIS data associated to the remaining 11 days are presented in Table 4. The MERIS level-1b radiances at 865 nm and 664 nm are averaged over a 3×3 pixels square. The reported root mean square (r.m.s.) values give an idea about the radiances dispersion within the window which is of the order of 1% or 2%. This dispersion is quite equivalent at 865 nm and 664 nm which may indicate that we observe case-2 waters for which no water leaving radiance structures appear at 664 nm. The MERIS data provide as well the geometrical conditions. The selection procedure of the MERIS images leads to collect data only for cameras 3 and 4. Cameras 1 and 5 were not selected because of larger view angles and camera 2 is most of the time contaminated by sun glint. In addition, the MERIS data provide meteorological parameters so that for each day we know the ozone content along the air column and the wind speed. In order to properly model the Fresnel reflection at sea surface, we have to use the wind matrix already generated for 7 wind speeds with a step of 1 m/s. For this purpose we select the wind file closest to the MERIS wind speed. Thus the uncertainty associated to the MERIS wind speed can be assumed to be lower than 1 m/s. Because of small wind speed values recorded we can neglect the contribution of the

Table 4
MERIS data for the 11 days finally selected

Site/Date	L_{13}^u	r.m.s.$_{13}$	L_7^u	r.m.s.$_7$	θ_S	φ_S	θ_v	φ_v	W (m/s)	O$_3$ (DU)
	(mW/m²/sr/nm)		(mW/m²/sr/nm)		(°)					
CA1028	3.16	0.07	10.75	0.15	49.7	156.0	12.7	284.4	2.0	278
VE1104	2.81	0.01	9.77	0.05	62.8	160.3	6.1	104.2	4.0	308
VE1113	5.06	0.05	13.77	0.08	64.5	165.2	19.7	287.2	1.1	336
CA1110	2.26	0.00	8.04	0.01	54.2	155.3	3.1	103.3	1.7	288
VE0810	5.84	0.06	15.85	0.08	35.4	139.7	1.6	104.7	0.6	318
VE0813	8.43	0.08	22.06	0.14	35.5	142.7	7.2	285.7	1.1	316
VE1025	2.96	0.04	9.78	0.10	58.8	163.1	15.8	286.7	1.5	322
VE1110	2.87	0.03	9.81	0.10	63.9	163.6	11.5	286.2	3.2	291
LP0820	8.25	0.05	19.34	0.07	32.3	129.4	2.6	103.5	4.8	288
MB1027	6.58	0.20	16.19	0.34	39.6	145.3	7.7	283.1	2.3	271
VE0823	7.63	0.04	20.32	0.13	39.7	140.8	14.7	103.2	1.7	310

The average values of MERIS TOA radiances and associated r.m.s. on a 3×3 pixels square are reported at MERIS bands 13 and 7. The geometrical conditions associated to the CIMEL platform location are indicated as well as the auxiliary meteorological data provided by MERIS such as the wind speed and the ozone content.

foam reflectance. We just assume standard ocean reflectance values that are 0% at all wavelengths except of 0.1% at 664 nm (Gordon et al., 1988).

Over the ocean the RTC requires as an input a solar zenith angle equal to a Gauss angle. We generally simulate one value of the TOA radiance per Gauss angle surrounding the MERIS solar zenith angle. After interpolation we get a TOA radiance that we can directly compare to MERIS measurements normalized to an extraterrestrial irradiance E_s equal to π.

We present now the results of the onboard calibration of MERIS at NIR wavelengths from band 14 (884 nm) to band 7 (664 nm). Table 5 is a summary of the results obtained for the 11 days selected. For each channel we report the predicted TOA radiances before and after correction that we

compare to the MERIS measurements. A correction of the simulated radiances according to Eq. (19) is possible for 8 days over 11 simply because of the index that is set to 1 or 2. We first analyse the results at 865 nm. Among the 8 days a correction is required only for 3 days. After being corrected, the TOA radiances are either in better agreement with MERIS measurements, for instance for CA1028, or as good as before correction, for instance for VE1110 and VE1113. In the case of CA1028 the discrepancy between simulations and MERIS was −10.5% before correction and is about +5.1% after correction. In the cases of VE1110 and VE1113 the simulations were about 5% greater than the MERIS measurements before correction. As the correction to be applied was about −10% in both cases (see Table 3), the simulations after correction were about 5% lower than

Table 5
Comparison between MERIS measurements and predicted TOA radiances for the 11 days selected

Site/Date	L_{14}^u (×10⁻²)		L_{13}^u (×10⁻²)		L_{12}^u (×10⁻²)		L_{10}^u (×10⁻²)		L_8^u (×10⁻²)		L_7^u (×10⁻²)	
CA1028	0.862	1.021	0.916	1.075	1.236	1.386	1.363	1.510	1.898	2.042	2.095	2.230
	0.957		*1.023*		*1.376*		*1.509*		*2.061*		*2.177*	
VE1104	0.896	0.896	0.958	0.958	1.292	1.221	1.415	1.333	1.964	1.837	2.153	2.004
	0.847		*0.906*		*1.203*		*1.316*		*1.873*		*1.971*	
VE1113	1.623	1.463	1.709	1.536	2.155	1.942	2.310	2.086	3.019	2.752	3.232	2.967
	1.532		*1.625*		*1.992*		*2.122*		*2.674*		*2.766*	
CA1110	0.684	0.684	0.729	0.729	0.944	0.945	1.099	1.036	1.563	1.457	1.736	1.630
	0.679		*0.726*		*0.982*		*1.090*		*1.532*		*1.617*	
VE0810	1.992	1.992	2.077	2.077	2.618	2.524	2.767	2.648	3.562	3.364	3.834	3.630
	1.859		*1.971*		*2.412*		*2.568*		*3.191*		*3.340*	
VE0813	2.878	2.878	3.026	3.026	3.796	3.441	4.094	3.639	5.271	4.479	5.657	4.866
	2.661		*2.839*		*3.451*		*3.691*		*4.452*		*4.652*	
VE1025	0.905	0.905	0.962	0.962	1.292	1.226	1.415	1.332	1.964	1.825	2.153	1.993
	0.899		*0.960*		*1.254*		*1.362*		*1.885*		*1.984*	
VE1110	0.904	0.823	0.957	0.871	1.253	1.142	1.367	1.249	1.879	1.737	2.049	1.883
	0.871		*0.923*		*1.191*		*1.295*		*1.886*		*1.973*	
LP0820	2.865	2.865	2.999	2.999	3.550	3.550	3.754	3.754	4.574	4.574	4.775	4.775
	2.921		*3.031*		*3.428*		*3.582*		*4.131*		*4.250*	
MB1027	2.739	2.739	2.831	2.831	3.350	3.350	3.538	3.538	4.369	4.369	4.629	4.629
	2.025		*2.130*		*2.478*		*2.617*		*3.150*		*3.276*	
VE0823	2.736	2.736	2.869	2.869	3.628	3.628	3.906	3.906	5.037	5.037	5.425	5.425
	2.411		*2.601*		*3.144*		*3.344*		*4.112*		*4.284*	

The simulated upward radiances are reported before and after correction for each NIR channel from 884 nm (band 14) to 664 nm (band 7). MERIS measurements are indicated in italic below the simulation values. The radiances are all normalized to an extraterrestrial irradiance E_s equal to π.

the MERIS measurements. At 865 nm the correction of simulated radiances is not often required, and when it is the agreement with MERIS measurements is better. At 664 nm it is different and a correction was required for the 8 days indexed as 1 or 2. This means that the aerosol phase function was not spectrally stable from 865 nm to 664 nm, what was expected as explained in Section 6. At 664 nm the agreement between simulations and MERIS is significantly better after correction except for CA2810 and VE1011 for which the agreement has the same magnitude, i.e. 3% and 4%, respectively. For the other days, the correction is really important as for VE1104 the difference between simulations and MERIS is +9.2% before correction and +1.7% after, for VE1113 it is +16.9% before and +7.3 after, for CA1011 it is

+7.4% before and −0.8% after, for VE0810 it is +14.8% before and +8.7% after, for VE0813 it is +21.6% before and +4.6% after and for VE1025 it is +8.5% before and +0.5% after. Now we focus on the 3 days indexed as 3 in the study. In this case we cannot correct the simulated radiances and the agreement between simulations and MERIS can be either good or bad. For instance at 865 nm there is an agreement of 1.1% between simulations and MERIS measurements for LP0820 whereas the discrepancies go up to 32.9% and 10.3% for MB1027 and VE0823, respectively. At 664 nm the discrepancies increase and we have a difference between simulations and MERIS of 12.4% for LP0820, of 41.3% for MB1027 and of 26.6% for VE0823. For these 3 days we do not know how to correct
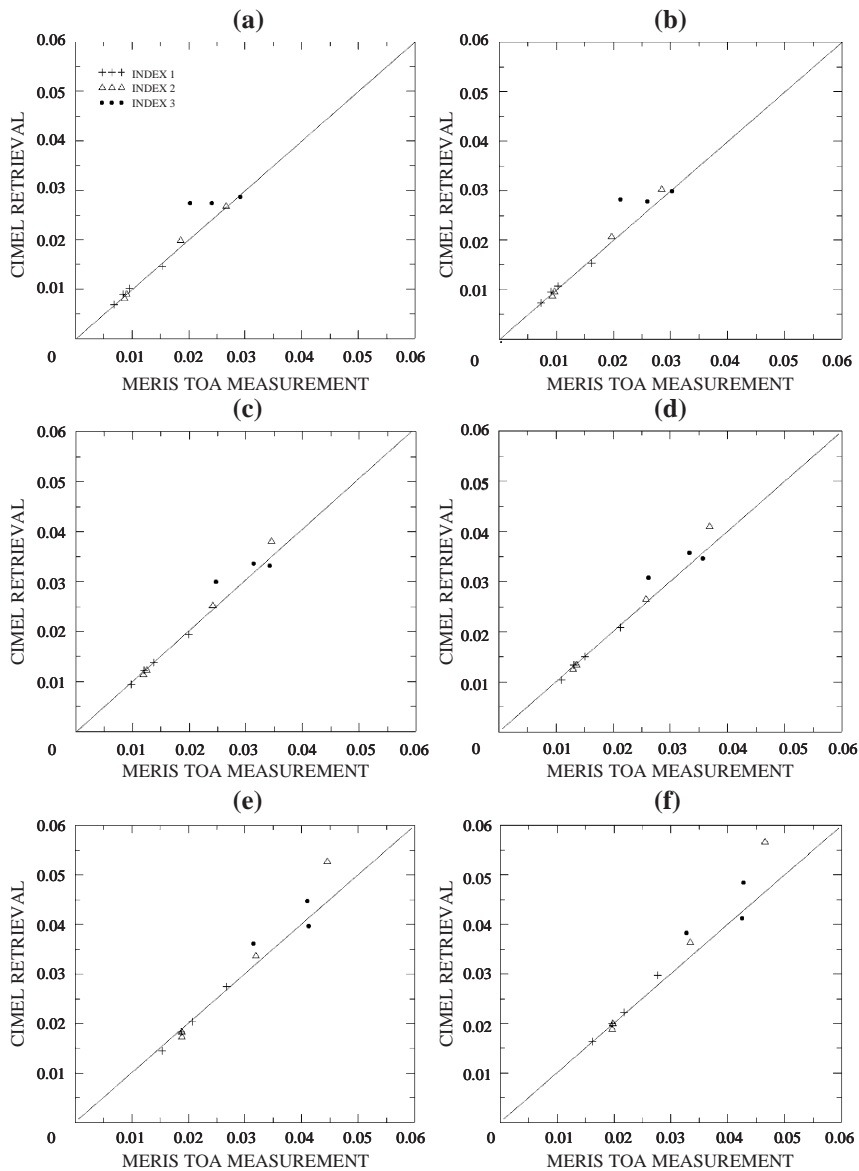

Fig. 7. Validation of the MERIS onboard calibration in the NIR at: (a) band 14, (b) band 13, (c) band 12, (d) band 10, (e) band 8, and (f) band 7. MERIS measurements and CIMEL retrievals are normalized radiances. CIMEL retrievals are computed using CIMEL measurements, AOT at MERIS overpass and "early morning" PPL radiances, as an input of the SOS code. Crosses, triangles, and circles represent points indexed as 1, 2, and 3, respectively.

for the variation of the aerosol phase function during the morning as we do not have other CIMEL principal plane measurements. In these conditions the agreement with MERIS can be either good or bad at 865 nm but is always bad at 664 nm. This shows the need of applying Eq. (19) to predict the upward radiances at 865 nm (temporal variation of the phase function) and at 664 nm (spectral variation of the phase function), and thus the need of having other sky radiance measurements to control the aerosol parameters derived in the early morning. At 884 nm an extrapolation of the correction from 865 nm was applied. At 778, 753, and 680 nm an interpolation between 865 and 664 nm was realized.

We represent now the comparisons between simulations and MERIS measurements at six wavelengths: 884 nm, 865 nm, 778 nm, 753 nm, 680 nm, and 664 nm in Fig. 7. The radiances are all normalized to an extraterrestrial irradiance E_s equal to π. We used three types of symbols: crosses for points indexed as 1, triangles for index 2, and dots for index 3. If we keep the points indexed as 3 the bias between MERIS measurements and CIMEL retrievals varies between −1.7% at 753 nm and −5.0% at 664 nm. The dispersion of the points that is two times the standard deviation never exceed 3.0%. These results are really satisfactory regarding the onboard calibration of MERIS but as previously shown we have a limited confidence in the predicted TOA radiances for the 3 days indexed as 3 so we decide to remove them for the MERIS calibration task in the NIR. If we keep only the points with the best confidence index (1 and 2) we improve significantly the results and the bias between MERIS measurements and CIMEL retrievals varies between −0.2% at 753 nm and −1.4% at 664 nm. In other words in these conditions we can retrieve MERIS TOA radiances using CIMEL ground-based measurements at better than 1.5% in the NIR. The dispersion is really satisfactory in all the cases as it is always lower than 3.0% (see Table 6) and in agreement with the accuracy of the vicarious calibration method used here for MERIS in the NIR (Santer & Martiny, 2003) which is between 2% and 3.6% (Martiny et al., submitted for publication).

Table 6
MERIS calibration results in the NIR

Band	Bias 1 (%)	Dispersion 1 (%)	Bias 2 (%)	Dispersion 2 (%)
14	−4.2	2.9	−1.2	1.6
13	−3.6	2.6	−1.3	1.7
12	−2.1	2.3	−0.4	1.5
10	−1.7	1.9	−0.2	1.6
8	−1.8	2.3	−0.5	2.5
7	−5.0	2.6	−1.4	2.7

Bias 1 indicates the relative difference between onboard and vicarious calibration. Dispersion 1 is the associated dispersion when we have 11 points, quality indexed as 1, 2 or 3. Bias 2 and Dispersion 2 indicate the same when we have 8 points, only indexed as 1 and 2.

8. Conclusion

In the current paper we report a clear methodology to perform vicarious calibration for the ocean colour sensors, and more specifically for MERIS, based on the determination of the atmospheric component using CIMEL ground-based measurements in the NIR. We use 5 months of data from July to November 2003 for five world sites that are Venice and Lampedusa (Italy), El Arenosillo (Spain), MOBY/Lanai and CalCOFI/San Nicolas (United States). The sites are all equipped with a CIMEL station that forms part of the AERONET network. The idea of associating the measured downward radiance to the radiance incoming to the satellite sensor at the same scattering angle is carefully examined. There are mainly three difficulties to overcome. Firstly, the relationship between the upward and downward signals as presented in this paper is true only under primary scattering approximation. As we use CIMEL radiance measurements that take into account the multiple scattering effects, we do have to select clear days to minimize these effects and we do have to correct them in order to be able using the primary scattering approximation. Secondly, it is difficult to get a same scattering angle observed from the ground and observed from space at the same time. We do have to take into account the temporal shift between the aerosol parameters derivation and the MERIS overpass. Thirdly, it is difficult to get the aerosol parameters at other wavelengths than 865 nm using the sky radiance measurements in the principal plane because of the Rayleigh and surface contributions that are more important. Hence, we present a clear protocol to derive the aerosol phase function from CIMEL sky radiance measurements at 865 nm, inspired from Santer and Martiny (2003), and we illustrate how to account for its temporal and spectral variations. From early morning to the time of MERIS overpass, we showed that the aerosol phase function did not present important temporal variation but did vary a lot from 865 to 664 nm, what was expectable. We took into account the temporal and spectral variations of the phase function applying a corrective factor determined from the downward sky radiance measurements performed with the CIMEL instrument. The correction factor defined at 865 and 664 nm to be either extrapolated at 884 nm or interpolated at 778, 753, and 680 nm seems appropriate regarding the results of the MERIS onboard calibration. Indeed, the main output of this study is the confirmation of the MERIS NIR calibration as we are able to retrieve MERIS TOA radiances using CIMEL ground-based measurements at better than 1.5% in the NIR, from 884 to 664 nm, with a maximum dispersion of 3.0%, what means within the 2.0% to 3.6% accuracy of the vicarious method we apply in this paper.

Nevertheless, it would be useful to directly derive the aerosol parameters from CIMEL sky radiances at 670 nm in

order to achieve the complete evaluation of the calibration method presented in this paper. Moreover, the vicarious calibration of MERIS in the NIR is based here on a severe selection process of CIMEL and MERIS data after which only 10% of the initial dataset remained. More efforts can certainly be devoted to the collection and reduction of more simultaneous data between the MERIS and CIMEL instruments. It is certainly relevant to perform an extensive analysis in order to see if no systematic biases occur versus the different parameters: site, period of the year.

The advantage of the method presented in this paper lies in the use of data from AERONET that are easily accessible. Thus, this strategy can be used by other groups and for other sensors to calibrate the NIR bands. On the other hand, this forward approach was devoted to the vicarious calibration in the red and the NIR bands. We think that this method can be also applied in the visible range if we introduce water leaving radiances. If we use a backward mode and rely on the MERIS radiometric calibration, we can also retrieve the water leaving radiances using the CIMEL-derived phase function and as a validation compare the results to the MERIS level-2 water leaving radiance products.

Acknowledgements

References

Antoine, D., & Chami, M. (2004). Vicarious calibration of MERIS level-1b observations: early results obtained at the Villefranche AERONET site. *Working meeting on MERIS and AATSR Calibration and Geophysical Validation (MAVT), ESRIN, Frascati, Italy, 20–24, October 2003*, Proceedings on CD-rom.

Barnes, R. A., & Eplee, Jr. R. E. (1996). The SeaWiFS solar diffuser. In R. A. Barnes, E.-N. Yeh, & R. E. Eplee Jr. (Eds.), *SeaWiFS Calibration Topics*, Part 1, NASA Technical Memo-104566 (NASA/GSFC-Goddard Space Flight Center), Greenbelt (MD), 39, pp. 1703–1712.

Barnes, R. A., Eplee, Jr., R. E., Patt, F. S., & McClain, C. R. (1999). Changes in the radiometric sensitivity of SeaWiFS determined from lunar and solar-based measurements. *Applied Optics 38*, 4649–4664.

Cox, C., & Munk, W. (1954). Measurements of roughness of the sea surface from photographs of the sun glitter. *Journal of the Optical Society of America 44*(11), 838–888.

Delwart, S., Preusker, R., Bourg, L., Santer, R., Ramon, D., & Fischer, J. (2003a). MERIS in-flight spectral calibration. *Journal of Atmospheric and Oceanic Technology* (submitted for publication).

Delwart, S., Bourg, L., & Huot, J. P. (1989). MERIS 1st year: Early calibration results. *Proceedings of the International Society for Optical Engineering (SPIE): Sensors, Systems and Next-Generation Satellite VII, Barcelona, Spain, vol. 5234* (pp. 379–390).

Deuzé, J. L., Herman, M., & Santer, R. (1989). Fourier series expansion of the transfer equation in the atmosphere-ocean system. *Journal of Quantitative Spectroscopy & Radiative Transfer 41*(6), 483–494.

Dilligeard, E., Zagolski, F., Fischer, J., & Santer, R. (2001). Uncertainties in radiative transfer computations: Consequences on the ocean colour products. *Proceedings of the International Society for Optical Engineering (SPIE): Ocean Remote Sensing and Applications, Hangzhu, China, vol. 4892* (pp. 546–556).

Fell, F., & Fischer, J. (2001). Numerical simulation of the light field in the atmosphere-ocean system using the matrix-operator method. *Journal of Quantitative Spectroscopy & Radiative Transfer 69*, 351–388.

Gordon, H. R. (1987). Calibration requirements and methodology for remote sensors viewing the ocean in the visible. *Remote Sensing of Environment 22*, 103–126.

Gordon, H. R. (1997). Atmospheric correction of ocean color imagery in the Earth Observing system era. *Journal of Geophysical Research 102*, 17081–17106.

Gordon, H. R., Brown, O. B., Evans, R. H., Brown, K. W., Smith, R. C., Baker, K. S., et al. (1988). A semi-analytic radiance model of ocean colour. *Journal of Geophysical Research 93*, 10909–10924.

Gordon, H. R., & Zhang, T. (1996). How well can radiance reflected from the ocean–atmosphere system be predicted from measurements at the surface. *Applied Optics 35*, 6527–6543.

Govaerts, Y. M., & Clerici, M. (2004). Comparison of MSG/SEVIRI calibration reference with MERIS BRF over bright desert calibration targets. Working meeting on MERIS and AATSR Calibration and Geophysical Validation (MAVT), ESRIN, Frascati, Italy, 20–24 October 2003, Proceedings on CD-rom.

Hagolle, O., & Cabot, F. (2004). Absolute calibration of MERIS using natural targets. Working meeting on MERIS and AATSR Calibration and Geophysical Validation (MAVT), ESRIN, Frascati, Italy, 20–24 October 2003, Proceedings on CD-rom.

Kieffer, H. H., & Widley, R. L. (1996). Establishing the moon as a spectral radiance standard. *Journal of Atmospheric and Oceanic Technology 13*, 360–375.

Martiny, N., Frouin, R., & Santer, R. (2004). Radiometric calibration of SeaWiFS in the near infrared. *Applied Optics*, (submitted for publication).

McClatchey, R. A., Fenn, R. W., Selby, J. E. A., Voltz, F. E., & Garing, J. S. (1971). Optical properties of the atmosphere. *Environmental Research Papers* (AFCRL-TR-71-0279, 354, Bedford, L.G., MA).

Meister, G., Abel, P., Barnes, R., Cooper, J., Davis, C., Fargion, G., et al. (2003). Comparison of spectral radiance calibrations at oceanographic and atmospheric research laboratories. *Metrologia 40*, S93–S96.

Merheim-Kealy, P., Huot, J. P., & Delwart, S. (1999). The MERIS Ground Segment. *International Journal of Remote Sensing 20*, 1703–1712.

Nieke, J., Hori, M., Höller, R., & Asanuma, I. (2004). Satellite sensor inter-calibration: A case of study for 28 March 2002. Working meeting on MERIS and AATSR Calibration and Geophysical Validation (MAVT), ESRIN, Frascati, Italy, 20–24 October 2003, Proceedings on CD-rom.

Parada, R., Thome, K. J., & Santer, R. (2004). Results of dark target vicarious calibration using Lake Tahoe. *Proceedings of the International Society for Optical Engineering (SPIE): Image and Signal Processing for Remote Sensing, EUROPTO—III, Taormina, Italy, vol. 2957* (pp. 332–343).

Rast, M., Bezy, J. L., & Bruzzi, S. (1999). The ESA Medium Resolution Imaging Spectrometer MERIS: A review of the instrument and its mission. *International Journal of Remote Sensing 20*, 1681–1702.

Santer, R., & Martiny, N. (2003). Sky radiance measurements for ocean colour calibration–validation. *Applied Optics 42*(6), 896–907.

Tanré, D., Deroo, C., Duhaut, P., Herman, M., Morcrette, J., Perbos, J., et al. (1990). Description of a computer code to simulate the satellite signal in the solar spectrum: 5S code. *International Journal of Remote Sensing 11*, 659–668.

Thuillier, G., Herse, M., Simon, P. C., Labs, D., Mandel, H., Gillotay, D., et al. (1998). The visible solar spectral irradiance from 350 to 850 nm as measured by the SOLSPEC spectrometer during the ATLAS-1 mission. *Solar Physics 177*, 41–61.

Vermote, E. F., Santer, R., Deschamps, P. Y., & Herman, M. (1992). In-flight calibration of large field of view sensors at short wavelengths using Rayleigh scattering. *International Journal of Remote Sensing 13*(18), 3409–3429.